PDRK: A General Kinetic Dispersion Relation Solver for Magnetized Plasma*

XIE Huasheng (谢华生), XIAO Yong (肖湧)

Institute for Fusion Theory and Simulation and the Department of Physics,
Zhejiang University, Hangzhou 310027, China

Abstract A general, fast, and effective approach is developed for numerical calculation of kinetic plasma linear dispersion relations. The plasma dispersion function is approximated by J-pole expansion. Subsequently, the dispersion relation is transformed to a standard matrix eigenvalue problem of an equivalent linear system. Numerical solutions for the least damped or fastest growing modes using an 8-pole expansion are generally accurate; more strongly damped modes are less accurate, but are less likely to be of physical interest. In contrast to conventional approaches, such as Newton's iterative method, this approach can give either all the solutions in the system or a few solutions around the initial guess. It is also free from convergence problems. The approach is demonstrated for electrostatic dispersion equations with one-dimensional and two-dimensional wavevectors, and for electromagnetic kinetic magnetized plasma dispersion relation for bi-Maxwellian distribution with relative parallel velocity flows between species.

Keywords: plasma physics, dispersion relation, kinetic, waves, instabilities, linear system, matrix eigenvalue

PACS: *52.27.Cm, 52.35.Qz, 52.35.−g, 52.35.Fp, 52.25.Dg*

DOI: 10.1088/1009-0630/18/2/01

(Some figures may appear in colour only in the online journal)

1 Introduction

Given the richness of waves and instabilities in astrophysical, space, laser, and laboratory plasmas, studying the corresponding linear dispersion relations of different plasma systems is of practical interest. However, except for some simple cases, the dispersion relations are usually too complicated to be solved either analytically or even numerically.

The multi-fluid plasma dispersion relation has been numerically solved using matrix method in a previous work, i.e., PDRF [1].

At present, several multi-component magnetized kinetic plasma dispersion relations solvers are available, such as WHAMP by Ronnmark [2,3], NHDS by Verscharen et al. [4], and solvers by Gary et al. [5,6], by Willes and Cairns [7,8] and by Lin et al. [9], among others. However, all these solvers obtain the dispersion relations from the determinant of the corresponding 3-by-3 dielectric tensor using a given initial guess. These solvers usually have difficulty in showing a complete picture of the modes in the system. Furthermore, these solvers may also suffer from convergence problems because the plasma dispersion function $Z(\zeta)$ and Bessel functions (especially in high-order cyclotron frequencies, e.g., $\omega > 10\Omega_c$, where Ω_c is the cyclotron frequency) have several solutions around a given frequency. Thus, a careful selection of the initial guess is required to make it converge to the solution we want.

In this work, we extend our previous work, a multi-fluid dispersion relation solver [1], to a general kinetic version, but still maintain the use of a full-matrix approach. In contrast to the straightforward matrix transformation in fluid case, two additional steps are required in the kinetic case: solving for the plasma dispersion function $Z(\zeta)$ and seeking an equivalent linear system. The first step is accomplished by J-pole expansion (Padé approximation) as used by Martin et al. [10] and Ronnmark [2,3]. The first step has also been used by Cereceda and Puerta [11] to solve the electrostatic 1D (ES1D) system. Physical interpretations of the Padé approximation of $Z(\zeta)$ are given by Tjulin et al. [12] and Robinson and Newman [13]. The second step is more difficult and should be treated on a case-to-case basis as we can see in the following sections.

2 Electrostatic systems

We start with simple electrostatic systems to show how our approach can be implemented.

*supported by the National Magnetic Confinement Fusion Science Program of China (Nos. 2015GB110003, 2011GB105001, 2013GB111000), National Natural Science Foundation of China (No. 91130031), the Recruitment Program of Global Youth Experts

2.1 Electrostatic 1D

First, we solve the simplest multi-component electrostatic 1D (ES1D) problem with drift Maxwellian distribution $f_{s0} = (\frac{m_s}{2\pi k_B T_s})^{1/2} \exp[-\frac{(v-v_{s0})^2}{2k_B T_s}]$. The dispersion relation is

$$D = 1 + \sum_{s=1}^{S} \frac{1}{(k\lambda_{Ds})^2}[1 + \zeta_s Z(\zeta_s)] = 0, \qquad (1)$$

where $\lambda_{Ds}^2 = \frac{\epsilon_0 k_B T_s}{n_s q_s^2}$, $v_{ts} = \sqrt{\frac{2k_B T_s}{m_s}}$ and $\zeta_s = \frac{\omega - k v_{s0}}{k v_{ts}}$. Unmentioned notations are standard. The plasma dispersion function $Z(\zeta) = \frac{1}{\sqrt{\pi}} \int_{-\infty}^{\infty} \frac{e^{-z^2}}{z-\zeta} dz$ can be approximated using J-pole expansion

$$Z(\zeta) \simeq Z_J(\zeta) = \sum_{j=1}^{J} \frac{b_j}{\zeta - c_j}, \qquad (2)$$

where $J = 8$ is used by Ronnmark [2,3] and $J = 2, 3, 4$ are provided by Martin et al. [10], producing accurate results for most domains (except $y < \sqrt{\pi} x^2 e^{-x^2}$ when $x \gg 1$, with $\zeta = x + iy$), especially in the upper plane. However, the method does not perform well for heavily damped modes, which are of little interest anyway. For completeness, the coefficients c_j and b_j for $J = 4$, $J = 8$ and $J = 12$ (see Appendix A) are provided in Table 1. Note the useful relations [2] $\sum_j b_j = -1$, $\sum_j b_j c_j = 0$ and $\sum_j b_j c_j^2 = -1/2$.

Combining Eqs. (1) and (2), yields

$$1 + \sum_s \sum_j \frac{b_{sj}}{(\omega - c_{sj})} = 0, \qquad (3)$$

with $b_{sj} = \frac{b_j c_j v_{ts}}{k\lambda_{Ds}^2}$ and $c_{sj} = k(v_{s0} + v_{ts} c_j)$. The solutions for the frequency $\omega = \omega_r + i\omega_i = \omega_r + i\gamma$ are usually complex numbers. An equivalent linear system can be obtained as follows:

$$\omega n_{sj} = c_{sj} n_{sj} + b_{sj} E, \qquad (4a)$$

$$E = -\sum_{sj} n_{sj}, \qquad (4b)$$

which is an eigenvalue problem of a $SJ \times SJ$ dimensional eigen matrix $\boldsymbol{M}$, i.e., $\omega \boldsymbol{X} = \boldsymbol{M}\boldsymbol{X}$, with $SJ = S \times J$ and $\boldsymbol{X} = \{n_{sj}\}$. The symbols n_{sj} and E used here do not have direct physical meanings but are analogy to the perturbed number density and electric field in fluid derivation of Langmuir wave. The singularity in the denominator of (3), which is encountered in conventional methods, can be canceled by using the transformation (4). Hence, the matrix method can easily support multi-component systems.

For Langmuir wave Landau damping, calculating the largest imaginary part solution using matrix method (ω^M) and the original $Z(\zeta)$ function (ω^Z) [14] are shown in Table 2. We can see that the result of the matrix method is accurate in 10^{-4} when $J = 8$ and the error for $J = 4$ is also small (10%). Thus, we have verified that our approach is feasible. In principle, infinite numbers of frequency solutions exist for a fixed wave vector k (the physical discussions can be found in Ref. [15] and references therein). Fig. 1 shows all the solutions of the matrix method and the solutions using $Z(\zeta)$ function for $k\lambda_{De} = 0.8$. The largest imaginary part (least damped) solutions (first solution) are almost identical, which is our objective. However, other heavily damped solutions should be excluded due to the poor approximation in those ranges. For example, the error for the second solution between the $Z(\zeta)$ solution and the $J = 8$ solution is around 10%, whereas the third solution is completely wrong for $J = 8$. Fortunately, for most studies, these heavily damped modes are of little interest. The $J = 12$ results can be more accurate (10^{-7}) as shown in Table 2 and Fig. 1. In principle, Eq. (1) has no singularity for $k \neq 0$. Given the existence of multiple solutions, if the initial guess is not good, then root finding cannot converge to the desired solutions.

For the two-frequency-scale ($s = e, i$, $m_e \ll m_i$) ion acoustic mode, besides the Langmuir mode $\omega = 2.0459 - 0.8513i$, the largest imaginary part solution obtained from the matrix method ($J = 8$) is also consistent with the solution obtained from the $Z(\zeta)$ function, e.g., $T_i = T_e$, $m_i = 1836 m_e$, $k\lambda_{De} = 1$, gives $\omega = 0.0420 - 0.0269i$. Hereafter, $J = 8$ will be used as default.

We further check the electron bump-on-tail mode (s=e,b), with $T_b = T_e$, $v_b = 5v_{te}$ and $n_b = 0.1 n_0$ ($n_e = n_0 - n_b$). Both $J = 8$ matrix method and root finding using $Z(\zeta)$ function give the same largest imaginary part solution $\omega = 0.9785 + 0.2000i$ for $k\lambda_{De} = 0.2$. The $J = 4$ matrix method gives $\omega = 0.9772 + 0.2076i$. Fig. 2 shows ω and γ vs. k for the above parameters, where the first three largest imaginary part solutions from the matrix method ($J = 8$) and one solution from $Z(\zeta)$ function are shown. ω^Z is identical to ω^M. However, different initial guesses should be tested to find other solutions when using the $Z(\zeta)$ function. By contrast, no initial guess is required when using the matrix method. Therefore, with matrix method, no important solutions are missed.

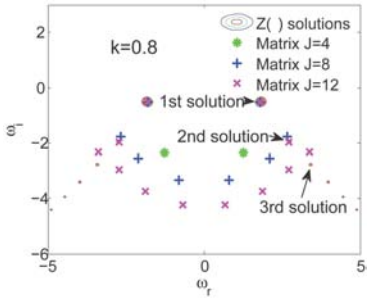

Fig.1 Comparison of all the solutions obtained from the matrix method and the $Z(\zeta)$ function. To avoid missing solutions, the $Z(\zeta)$ function solutions are shown by contour plot of Eq. (1) $|D(\omega_r, \omega_i)| = 0$ in the complex plane, which can show the distribution of all solutions in the complex plane directly. The arrows in the figures point out the positions of the first three solutions. We can see that $J = 4, 8, 12$ all can reproduce the first solution, but only $J = 12$ can reproduce the second solution accurately

Table 1. The coefficients c_j and b_j for $J = 4$ [10], $J = 8$ [2] and $J = 12$ (Appendix A) under J-pole approximations of $Z(\zeta)$, where the asterisk denotes complex conjugation

$J = 4$	b_1=0.546796859834032+0.037196505239277i	c_1=1.23588765343592−1.21498213255731i
	b_2=−1.046796859834027+2.101852568038518i	c_2=−0.378611612386277−1.350943585432730i
	$b(3:4)$=$b^*(1:2)$	$c(3:4)$=$-c^*(1:2)$
$J = 8$	b_1=−1.734012457471826E−2−4.630639291680322E−2i	c_1=2.237687789201900−1.625940856173727i
	b_2=−7.399169923225014E−1+8.395179978099844E−1i	c_2=1.465234126106004−1.789620129162444i
	b_3=5.840628642184073+9.536009057643667E−1i	c_3=0.8392539817232638−1.891995045765206i
	b_4=−5.583371525286853−1.120854319126599E1i	c_4=0.2739362226285564−1.941786875844713i
	$b(5:8)$=$b^*(1:4)$	$c(5:8)$=$-c^*(1:4)$
$J = 12$	b_1=−0.004547861216840+0.000621096229879i	c_1=2.978429162453205−2.049696666440972i
	b_2=0.215155729059403−0.201505401705763i	c_2=−2.256783783969929−2.208618419119446i
	b_3=0.439545043457674−4.161084685092405i	c_3=1.673799856114519−2.324085194217706i
	b_4=−20.216967308177410+12.885503528244977i	c_4=1.159032034062764−2.406739409567887i
	b_5=67.081488119986460−20.846345891864550i	c_5=−0.682287637027822 −2.460365014999888i
	b_6=−4.801467372237129e+01−1.072756140299431e+02i	c_6=0.225365375295874−2.486779417872603i
	$b(7:12)$=$b^*(1:6)$	$c(7:12)$=$-c^*(1:6)$

Table 2. Comparison of the Landau damping solutions using the matrix method and the original $Z(\zeta)$ function. Here, ω is normalized by $\omega_{\rm pe} = \sqrt{n_{\rm e}e^2/\epsilon_0 m_{\rm e}}$

$k\lambda_{\rm De}$	$\omega_{\rm r}^M(J=4)$	$\omega_{\rm i}^M(J=4)$	$\omega_{\rm r}^M(J=8)$	$\omega_{\rm i}^M(J=8)$	$\omega_{\rm r}^M(J=12)$	$\omega_{\rm i}^M(J=12)$	$\omega_{\rm r}^Z$	$\omega_{\rm i}^Z$
0.1	0.9956	9.5E-3	1.0152	1.7E−5	1.0152	9.5E−8	1.0152	−4.8E−15
0.5	1.4235	−0.1699	1.4156	−0.1534	1.4157	−0.1534	1.4157	−0.1534
1.0	2.0170	−0.8439	2.0459	−0.8514	2.0458	−0.8513	2.0458	−0.8513
2.0	3.2948	−2.6741	3.1893	−2.8272	3.1891	−2.8272	3.1891	−2.8272

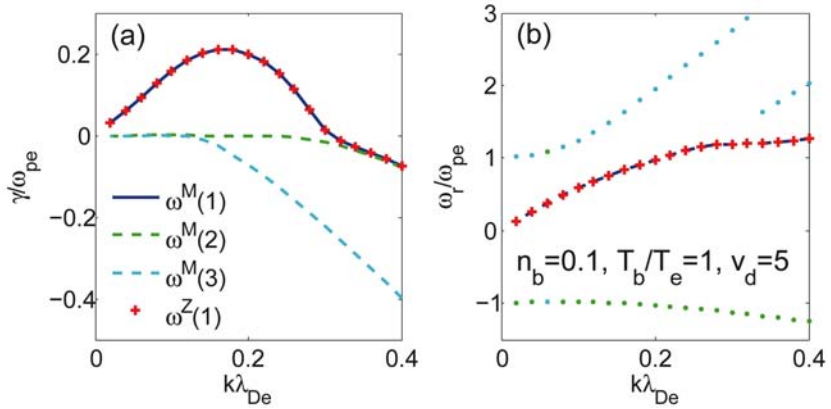

Fig.2 Comparison of the first three (ω^M) largest imaginary part solutions obtained from the matrix method ($J = 8$) and one solution (ω^Z) obtained from $Z(\zeta)$ function for the bump-on-tail parameters. The matrix method reproduces one of the $Z(\zeta)$ function solutions accurately and can also give other solutions directly

2.2 Harris dispersion relation

We go further to solve a more complicated example, including the n-th ($n = -\infty$ to ∞) order cyclotron frequency, i.e., the electrostatic 3D-magnetized (ES3D) Harris dispersion relation [16]

$$D = 1 + \sum_{s=1}^{S} \frac{1}{(k\lambda_{\rm Ds})^2}\Big[1 + \frac{\omega - k_z v_{s0} - n\Omega_s + \lambda_T n\Omega_s}{k_z v_{zts}} \times \sum_{n=-\infty}^{\infty} \Gamma_n(b_s) Z(\zeta_{sn})\Big] = 0, \quad (5)$$

where, $\lambda_{{\rm D}s}^2 = \frac{\epsilon_0 k_{\rm B} T_{zs}}{n_{s0} q_s^2}$, $v_{\rm ts} = \sqrt{\frac{2k_{\rm B}T_s}{m_s}}$, $\lambda_T = T_z/T_\perp$, $\zeta_{sn} = \frac{\omega - k_z v_{s0} - n\Omega_s}{k_z v_{zts}}$, $\Gamma_n(b) = I_n(b){\rm e}^{-b}$, $b_s = k_\perp^2 \rho_{cs}^2$, $\rho_{\rm cs} = \sqrt{\frac{v_{\perp ts}^2}{\Omega_s}}$, I_n is the modified Bessel function, and the equilibrium distribution is assumed to be drift bi-Maxwellian $f_{s0} = f_\perp(v_\perp) f_z(v_z)$, with $f_\perp = \frac{m_s}{2\pi k_{\rm B} T_{s\perp}} \exp[-\frac{m_s v_\perp^2}{2k_{\rm B}T_{s\perp}}]$ and $f_z = (\frac{m_s}{2\pi k_{\rm B} T_{s\perp}})^{1/2} \exp[-\frac{m_s (v_\parallel - v_{s0})^2}{2k_{\rm B}T_{sz}}]$. The background magnetic field is assumed to be $\mathbf{B}_0 = (0, 0, B_0)$, and the wave vector $\mathbf{k} = (k_x, 0, k_z) = (k\sin\theta, 0, k\cos\theta)$, which gives $k_\perp = k_x$ and $k_\parallel = k_z$.

This dispersion relation contains infinite-order sum-

mation of Bessel functions. However, Eq. (5) is very similar to Eq. (1). Thus, the transformation to an equivalent linear system/matrix is the same and straightforward. In the computation, we only keep the first N Bessel functions, i.e., $n{=}{-}N$ to N. The dimensions of the eigen matrix is $SNJ \times SNJ$, with $SNJ = S \times (2N+1) \times J$. The singularity for $k_z \to 0$ around $\omega - n\Omega_{cs} \to 0$ in Eq. (5) is removed after the transformation.

2.2.1 Electron Bernstein modes

First, we benchmark the electron Bernstein modes (s=e). The result is shown in Fig. 3(a), with parameter $\omega_{pe} = 2.5\omega_{ce}$. For the modes with frequency $\omega < 6\omega_c$, considering the $N = 10$-order Bessel functions is accurate enough. The upper hybrid frequency calculated at the cold limit is $\omega_{UH} = \sqrt{\omega_c^2 + \omega_p^2} = 2.69$, which is consistent with the matrix solution in the limit $k_\perp \rho_c \to 0$. Fig. 3(a) also agrees with Fig. 9.8 in Ref. [16]. The corresponding ES1D3V particle-in-cell (PIC) simulation (ion immobile, $k = k_\perp$) verification is also shown in Fig. 3(b), where good agreement is observed. Standard PIC simulation method [17] is used here. The contour plot of the spectra in Fig. 3(b) is calculated by Fourier transformation of the electrostatic potential $\delta\phi(x,t)$ to $\delta\hat{\phi}(k,\omega)$.

2.2.2 Anisotropic instabilities

Second, we benchmark the anisotropic instabilities with Ref. [18]. The contour plot of the growth rate γ/ω_c is shown in Fig. 4, with $\omega_p = \omega_c$ and $N = 4$. The results agree with Fig. 2 in Ref. [18].

3 Electromagnetic dispersion relation

In the above section, we have shown that the matrix method can solve the kinetic dispersion relations. In addition, the results are accurate enough even if we used Padé approximation to the Z function, which gives us enough confidence with the approach to extend its application further to the magnetized electromagnetic (EM3D) dispersion relations, which has not been solved well using conventional approaches.

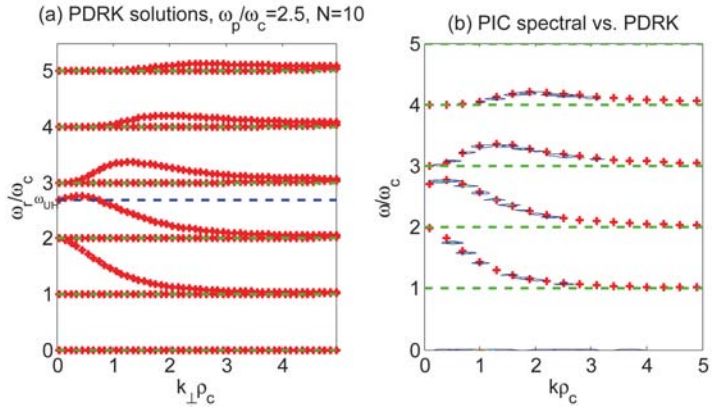

Fig.3 The electron Bernstein modes calculated from the Harris dispersion relation using the matrix method (red '+'). The green dash lines are $\omega = n\omega_c$. The upper hybrid frequency calculated at the cold limit is $\omega_{UH} = \sqrt{\omega_c^2 + \omega_p^2} = 2.69$ (blue dash line), which agrees with the matrix solution in the limit $k_\perp \rho_c \to 0$. The plasma dispersion relation kinetic version (PDRK-ES3D) solutions also agree with the contour plot of the PIC spectra (b)

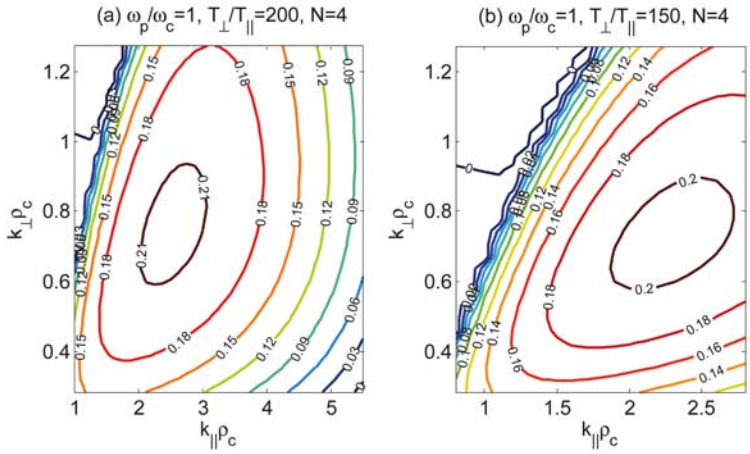

Fig.4 The anisotropic instabilities (growth rate γ/ω_c) calculated from the Harris dispersion relation using the matrix method. The results agree with Ref. [18]

3.1 The dispersion relation

The equilibrium distribution is still assumed to be drift bi-Maxwellian as in section 2.2, and also $\mathbf{B}_0 = (0, 0, B_0)$ and $\mathbf{k} = (k_x, 0, k_z)$. The dispersion relation can be derived as [19]

$$\begin{vmatrix} K_{xx} - \frac{c^2k^2}{\omega^2}\cos^2\theta & K_{xy} & K_{xz} + \frac{c^2k^2}{\omega^2}\sin\theta\cos\theta \\ K_{yx} & K_{yy} - \frac{c^2k^2}{\omega^2} & K_{yz} \\ K_{zx} + \frac{c^2k^2}{\omega^2}\sin\theta\cos\theta & K_{zy} & K_{zz} - \frac{c^2k^2}{\omega^2}\sin^2\theta \end{vmatrix} = 0, \tag{6}$$

with $\boldsymbol{K} = \boldsymbol{I} + \sum_s \frac{\omega_{\mathrm{p}s}^2}{\omega^2}\Big[\sum_n \big\{\zeta_0 Z(\zeta_n) - (1 - \frac{1}{\lambda_T})[1 + \zeta_n Z(\zeta_n)]\big\}\boldsymbol{X}_n + 2\eta_0^2\lambda_T\boldsymbol{L}\Big]$, where

$$\boldsymbol{X}_n = \begin{pmatrix} n^2\Gamma_n/b & \mathrm{i}n\Gamma_n' & -(2\lambda_T)^{1/2}\eta_n\frac{n}{\alpha}\Gamma_n \\ \mathrm{i}n\Gamma_n' & n^2/b\Gamma_n - 2b\Gamma_n' & \mathrm{i}(2\lambda_T)^{1/2}\eta_n\alpha\Gamma_n' \\ -(2\lambda_T)^{1/2}\eta_n\frac{n}{\alpha}\Gamma_n & -\mathrm{i}(2\lambda_T)^{1/2}\eta_n\alpha\Gamma_n' & 2\lambda_T\eta_n^2\Gamma_n \end{pmatrix}, \tag{7}$$

$\eta_n = \frac{\omega + n\Omega}{k_z v_{Tz}}$, $\lambda_T = \frac{T_z}{T_\perp}$, $b = (\frac{k_x v_{T\perp}}{\Omega})^2$, $\alpha = \frac{k_x v_{T\perp}}{\Omega}$, $v_{T_z}^2 = \frac{k_{\mathrm{B}}T_z}{m}$, $v_{T_\perp}^2 = \frac{k_{\mathrm{B}}T_\perp}{m}$ and the matrix components of $\boldsymbol{L}$ are all zero, except for $L_{zz} = 1$.

3.2 The linear transformation

To seek an equivalent linear system, the Maxwell's equations

$$\partial_t\mathbf{E} = c^2\nabla\times\mathbf{B} - \mathbf{J}/\epsilon_0, \tag{8a}$$

$$\partial_t\mathbf{B} = -\nabla\times\mathbf{E}, \tag{8b}$$

do not need to be changed. We only need to seek a new linear system for $\mathbf{J} = \overleftrightarrow{\sigma}\cdot\mathbf{E}$. It is easy to find that after J-pole expansion, the relations between $\mathbf{J}$ and $\mathbf{E}$ has the following form:

$$\begin{pmatrix} J_x \\ J_y \\ J_z \end{pmatrix} = \begin{pmatrix} a_{11} + \sum_{snjm}\frac{b_{snjm11}}{\omega - c_{snjm11}} & a_{12} + \sum_{snjm}\frac{b_{snjm12}}{\omega - c_{snjm12}} & a_{13} + \sum_{snjm}\frac{b_{snjm13}}{\omega - c_{snjm13}} \\ a_{21} + \sum_{snjm}\frac{b_{snjm21}}{\omega - c_{snjm21}} & a_{22} + \sum_{snjm}\frac{b_{snjm22}}{\omega - c_{snjm22}} & a_{23} + \sum_{snjm}\frac{b_{snjm23}}{\omega - c_{snjm23}} \\ a_{31} + \sum_{snjm}\frac{b_{snjm31}}{\omega - c_{snjm31}} & a_{32} + \sum_{snjm}\frac{b_{snjm32}}{\omega - c_{snjm32}} & a_{33} + \sum_{snjm}\frac{b_{snjm33}}{\omega - c_{snjm33}} + d_{33}\omega \end{pmatrix}\begin{pmatrix} E_x \\ E_y \\ E_z \end{pmatrix}. \tag{9}$$

Fortunately, noting the relations in Z function ($\sum_j b_j = -1$, $\sum_j b_j c_j = 0$ and $\sum_j b_j c_j^2 = -1/2$) and in Bessel functions [$\sum_{n=-\infty}^{\infty} I_n(b) = \mathrm{e}^b$, $\sum_{n=-\infty}^{\infty} nI_n(b) = 0$, $\sum_{n=-\infty}^{\infty} n^2 I_n(b) = b\mathrm{e}^b$], we find that $a_{ij} = 0$ $(i, j = 1, 2, 3)$ and $d_{33} = 0$. Eq. (9) can be changed further to

$$\begin{pmatrix} J_x \\ J_y \\ J_z \end{pmatrix} = -\begin{pmatrix} \frac{b_{11}}{\omega} + \sum_{snj}\frac{b_{snj11}}{\omega - c_{snj}} & \frac{b_{12}}{\omega} + \sum_{snj}\frac{b_{snj12}}{\omega - c_{snj}} & \frac{b_{13}}{\omega} + \sum_{snj}\frac{b_{snj13}}{\omega - c_{snj}} \\ \frac{b_{21}}{\omega} + \sum_{snj}\frac{b_{snj21}}{\omega - c_{snj}} & \frac{b_{22}}{\omega} + \sum_{snj}\frac{b_{snj22}}{\omega - c_{snj}} & \frac{b_{23}}{\omega} + \sum_{snj}\frac{b_{snj23}}{\omega - c_{snj}} \\ \frac{b_{31}}{\omega} + \sum_{snj}\frac{b_{snj31}}{\omega - c_{snj}} & \frac{b_{32}}{\omega} + \sum_{snj}\frac{b_{snj32}}{\omega - c_{snj}} & \frac{b_{33}}{\omega} + \sum_{snj}\frac{b_{snj33}}{\omega - c_{snj}} \end{pmatrix}\begin{pmatrix} E_x \\ E_y \\ E_z \end{pmatrix}. \tag{10}$$

Combining Eqs. (8) and (9), the equivalent linear system for (6) can be obtained as

$$\begin{cases} \omega v_{snjx} &= c_{snj}v_{snjx} + b_{snj11}E_x + b_{snj12}E_y + b_{snj13}E_z, \\ \omega j_x &= b_{11}E_x + b_{12}E_y + b_{13}E_z, \\ J_x &= j_x + \sum_{snj} v_{snjx}, \\ \omega v_{snjy} &= c_{snj}v_{snjy} + b_{snj21}E_x + b_{snj22}E_y + b_{snj23}E_z, \\ \omega j_y &= b_{21}E_x + b_{22}E_y + b_{23}E_z, \\ J_y &= j_y + \sum_{snj} v_{snjy}, \\ \omega v_{snjz} &= c_{snj}v_{snjz} + b_{snj31}E_x + b_{snj32}E_y + b_{snj33}E_z, \\ \omega j_z &= b_{31}E_x + b_{32}E_y + b_{33}E_z, \\ J_z &= j_z + \sum_{snj} v_{snjz}, \\ \omega E_x &= -c^2k_zB_y - J_x/\epsilon_0, \\ \omega E_y &= c^2k_zB_x - c^2k_xB_z - J_y/\epsilon_0, \\ \omega E_z &= c^2k_xB_y - J_z/\epsilon_0, \\ \omega B_x &= k_zE_y, \\ \omega B_y &= -k_zE_x + k_xE_z, \\ \omega B_z &= -k_zE_y, \end{cases} \tag{11}$$

which yields a sparse matrix eigenvalue problem. Again, the symbols v_{snjx}, $j_{x,y,z}$ and $J_{x,y,z}$ used here do not have direct physical meanings but are analogy to the perturbed velocity and current density in the fluid [1] derivations of plasma waves. The elements of the eigenvector $(E_x, E_y, E_z, B_x, B_y, B_z)$ still represent the original electric and magnetic fields. Thus, the polarization of the solutions can also be obtained in a straightforward manner. The dimension of the matrix is $NN = 3 \times (SNJ + 1) + 6 = 3 \times [S \times (2 \times N + 1) \times J + 1] + 6$. The coefficients are

$$\left\{\begin{array}{rcl}
b_{snj11} & = & \omega_{\rm ps}^2 b_j (1 - k_z b_{j0}/c_{snj}) n^2 \Gamma_n / b_s, \\
b_{11} & = & \sum_{snj} \omega_{\rm ps}^2 b_j (k_z b_{j0}/c_{snj}) n^2 \Gamma_n / b_s, \\
b_{snj12} & = & \omega_{\rm ps}^2 b_j (1 - k_z b_{j0}/c_{snj}) {\rm i} n \Gamma'_n, \\
b_{12} & = & \sum_{snj} \omega_{\rm ps}^2 b_j (k_z b_{j0}/c_{snj}) {\rm i} n \Gamma'_n, \\
b_{snj21} = -b_{snj12}, & & b_{21} = -b_{12}, \\
b_{snj22} & = & \omega_{\rm ps}^2 b_j (1 - k_z b_{j0}/c_{snj}) (n^2 \Gamma_n / b_s - 2 b_s \Gamma'_n), \\
b_{22} & = & \sum_{snj} \omega_{\rm ps}^2 b_j (k_z b_{j0}/c_{snj}) (n^2 \Gamma_n / b_s - 2 b_s \Gamma'_n), \\
b_{snj13} & = & \omega_{\rm ps}^2 b_j [c_j/\lambda_{Ts} - n\omega_{cs} b_{j0}/(c_{snj} v_{tzs})] \Gamma_n / b_s, \\
b_{13} & = & \sum_{snj} \omega_{\rm ps}^2 b_j [n\omega_{cs} b_{j0}/(c_{snj} v_{tzs})] \Gamma_n / b_s, \\
b_{snj31} = b_{snj13}, & & b_{31} = b_{13}, \\
b_{snj23} & = & -{\rm i}\omega_{\rm ps}^2 b_j [c_j/\lambda_{Ts} - n\omega_{cs} b_{j0}/(c_{snj} v_{tzs})] \sqrt{(2\lambda_{Ts})} \Gamma'_n b_s, \\
b_{23} & = & -{\rm i} \sum_{snj} \omega_{\rm ps}^2 b_j [n\omega_{cs} b_{j0}/(c_{snj} v_{tzs})] \sqrt{(2\lambda_{Ts})} \Gamma'_n b_s, \\
b_{snj32} = -b_{snj23}, & & b_{32} = -b_{23}, \\
b_{snj33} & = & \omega_{\rm ps}^2 b_j [(v_{s0}/v_{tzs} + c_j) c_j/\lambda_{Ts} - n\omega_{cs} b_{j0} (1 + n\omega_{cs}/(c_{snj} v_{tzs}^2)/k_z] 2\lambda_{Ts} \Gamma_n, \\
b_{33} & = & \sum_{snj} \omega_{\rm ps}^2 b_j [n^2 b_{j0}/(c_{snj} v_{tzs}^2 k_z)] 2\lambda_{Ts} \Gamma_n, \\
c_{snj} & = & k_z c_j v_{tzs} + k_z v_{s0} - n\omega_{cs},
\end{array}\right. \tag{12}$$

where $b_{j0} = v_{s0} + (1 - 1/\lambda_{Ts}) c_j v_{tzs}$.

If $a_{ij} \neq 0$, then the equivalent linear transformation is still straightforward. However, the eigenmatrix will not be sparse (the ES1D and ES3D eigenmatrices in section 2 are not sparse, see Appendix B for the sparse ones). If $d_{33} \neq 0$, then the equivalent linear transformation will be more complicated. For our purposes, we do not need to discuss these cases.

4 Benchmarks and applications

The PDRK code (see https://github.com/hsxie/pdrk or http://hsxie.me/codes/pdrk/. Three versions are included at present: ES1D, ES3D, EM3D. If not specified, PDRK represents PDRK-EM3D.) is developed based on the above method. We now benchmark this code and show some typical applications. Default parameters for the succeeding cases are $c^2 = 10^4$, $B_0 = 1$, $m_{\rm e} = 1$, $q_{\rm e} = -1$, $\epsilon_0 = 1$.

4.1 Benchmark with fluid solver PDRF

First, we compare PDRK with the fluid solver PDRF [1]. Fig. 5 shows the results at the cold limit with parallel propagation ($k = k_z$). In PDRF, we set $T_{\rm e} = T_{\rm i} = 0$; in PDRK, we set $T_{\rm e} = T_{\rm i} = 0.01 \ll 1$. The real frequencies in PDRK (ω^K) and in PDRF (ω^F) are almost identical. However, the kinetic damping is not zero as in the fluid framework, especially the cyclotron damping for ions, which is apparent in Panel (b). This cyclotron damping is not predicted in the fluid theory.

Fig. 6 shows the results for warm plasma with perpendicular propagation. We see that the fluid version results are close to the kinetic version results at small k ($kc/\omega_{\rm ce} < 2$), but deviates at large k. This kinetic correction (Bernstein modes) from the harmonics of the cyclotron frequency is also not predicted in fluid theory.

A further test (Fig. 11) of the electron Bernstein modes, which is quasi-electrostatic and makes use of the parameters in Fig. 3, gives similar results between PDRK-EM3D and PDRK-ES3D. Thus, for this step, PDRK-EM3D works well.

4.2 Parallel propagation kinetic modes

The kinetic dispersion relation for parallel propagation modes [16,19] is relatively simple to solve because the effects of the higher-order cyclotron harmonics are zero. One branch is the same as the ES1D dispersion relation Eq. (1). The other two branches are given by

$$D(k,\omega) = 1 - \frac{k^2 c^2}{\omega^2} + \sum_s \frac{\omega_{\rm ps}^2}{\omega k v_{\rm ts}} Z\left(\frac{\omega \pm \omega_{\rm cs}}{k v_{ts}}\right) = 0. \tag{13}$$

Eqs. (1) and (13) are solved by root finding with the original Z function [20] and comparing with PDRK. A typical result is shown in Fig. 7. We find a good agreement between the two methods. In addition, the ion and electron cyclotron damping and the Landau damping are clearly shown. However, too many extraneous solutions exist in the PDRK results. Most of the heavily damped solutions are not shown in the figure. The solutions represented by the red solid line ($\omega^{\rm R}$) in the figure should be real solutions. At large k (e.g., $kc/\omega_{\rm ce} > 7$, where PDRK solutions still agree with $\omega^{\rm R}$ but not shown), the damping rates of several artificial solutions are smaller than $\omega^{\rm R}$, which makes it difficult to separate the real and the artificial solutions directly.

To this step, PDRK-EM3D works well for $T_{s\parallel} = T_{s\perp}$ and $v_{s0} = 0$. For the heavily damped solutions, keeping

all the interesting solutions while removing the artificial solutions is usually not easy. Besides the heavily damped solutions, the artificial solutions roughly satisfy $\omega_{\rm r} - n\Omega_{\rm c} \propto k_{\|}$ and $\gamma \propto k_{\|}$ (come from the poles $\zeta - c_j \to 0$ of J-pole expansion). Therefore, this process can also be used to remove some of the artificial solutions. Several of the ES3D artificial solutions in Fig. 8 are removed based on this property.

When a sparse matrix is not used, the computation time is around $O(NN^{\alpha})$ with $2 < \alpha < 3$ and the memory required is around $O(NN^2)$. A typical personal computer with 4 GB memory can calculate NN up to 7000 ($NN = 7000$, $S = 2$, $J = 8$, give $N \simeq 60$) in minutes. Thus, for modes with frequency $\omega < 60\Omega_{\rm ci}$, all the solutions in the system can be obtained easily. When a sparse matrix is used, NN can reach up to 10^6. Thus N can be up to 10^4. The standard sparse matrix algorithm can solve one or several solutions around the initial guess.

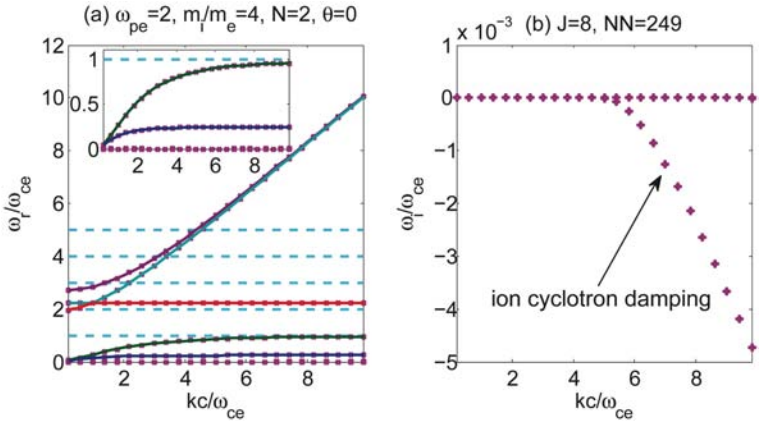

Fig.5 PDRK (dot) vs. PDRF (solid line), cold ($T_{\rm e} = T_{\rm i} = 0.01$), parallel propagation. The real frequencies in both solvers are almost identical. However, the cyclotron damping is not predicted in PDRF

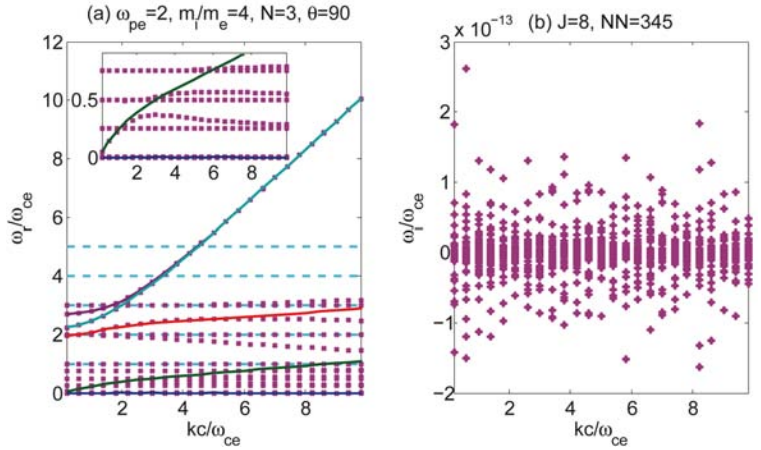

Fig.6 PDRK (dot) vs. PDRF (solid line), warm ($T_{\rm e} = T_{\rm i} = 100$), perpendicular propagation. The positive $\gamma \simeq 10^{-13}$ comes from numerical error of $J = 8$

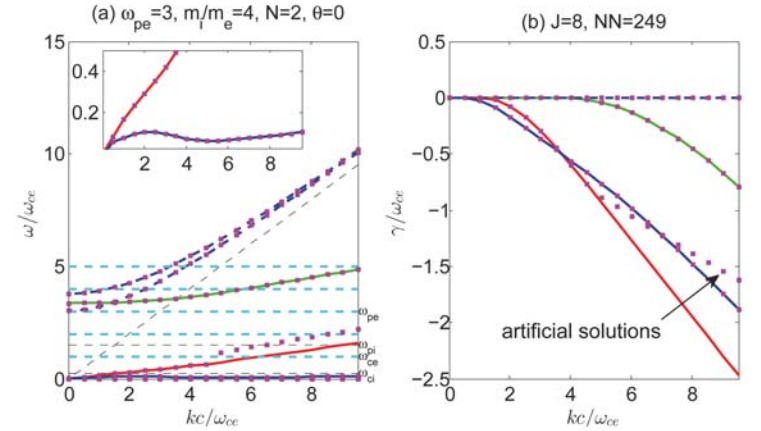

Fig.7 PDRK solutions (dot) vs. Z function solutions (solid and green dash lines), warm ($T_{\rm e} = T_{\rm i} = 400$), parallel propagation. Heavily damped (both real and artificial) solutions are not shown

4.3 Landau damping of lower hybrid wave

Now, we benchmark the Landau damping of lower hybrid wave (LHW) using a real mass ratio $m_\mathrm{i}/m_\mathrm{e} = 1836$, where large N should be used to make the solutions convergent. For the electrostatic case, with $k^2\rho_\mathrm{e}^2 \ll 1$, $\omega_\mathrm{ci} \ll \omega \ll \omega_\mathrm{pe}$ and $k_\parallel/k \ll 1$, the analytical solution $\omega = (\omega_\mathrm{r}, \gamma)$ for LHW can be found in Ref. [21]. We use the same parameters ($\omega_\mathrm{pe} = \omega_\mathrm{ce}$, $k_\parallel/k_\perp = 0.066$, $T_\mathrm{e} = T_\mathrm{i}$) as in Fig. 1 of Ref. [21] for the benchmark because this has also been verified by first-principle PIC simulations in that paper. The results are shown in Fig. 8, where the electrostatic assumption works well for large k. For small k ($k_\perp\rho_\mathrm{ce} < 0.04$), the electromagnetic effects should be included, which is consistent with the results on fluid frequency and polarization in a previous study [1].

Note that several limits for the parameters have been used to obtain the analytical solution. Similar limits have also been used for warm EM LHW (see e.g., Ref. [8]). Therefore, it is not surprising that the analytical solution does not hold for large k ($k_\perp\rho_\mathrm{ce} > 0.4$) in the figure. For fusion (e.g., Ref. [22]) or space studies, the approximate analytical solution is not always valid. Thus, PDRK can serve as a numerical tool for a wider range of parameters.

For this step, we have shown that PDRK-EM3D works well also for $N \geq 50$ by using a sparse matrix, though an initial guess is required and the computational time is longer.

4.4 Firehose and mirror modes

Firehose and mirror modes are typical unstable modes driven by pressure anisotropic $T_\parallel \neq T_\perp$. For cold electrons, the approximate analytical kinetic dispersion relations for the firehose mode is $\omega^2 = \omega_\mathrm{A}^2[\frac{b_\mathrm{i}}{1-\Gamma_0(b_\mathrm{i})} + \frac{\beta_{\mathrm{i}\perp}-\beta_{\mathrm{i}\parallel}}{2}]$. For the mirror mode, it is $\zeta_\mathrm{i}Z(\zeta_\mathrm{i}) = \frac{\eta_\mathrm{i}}{\beta_{\mathrm{i}\perp}\Gamma_1(b_\mathrm{i})} - (1-\eta_\mathrm{i})$, with $\eta_\mathrm{i} = \beta_{\mathrm{i}\parallel}/\beta_{\mathrm{i}\perp}$.

A typical result is shown in Fig. 9, where $\omega_\mathrm{pe}/\omega_\mathrm{ce} = 2$, $m_\mathrm{i}/m_\mathrm{e} = 100$, $\omega_\mathrm{A} = k_\parallel v_\mathrm{A} = 0.01\omega_\mathrm{ci}$ and $\beta_\mathrm{e} = 0.08$. The PDRK solutions agree with the analytical solutions for both the firehose and mirror modes. The small deviation is not surprising because the analytical solutions are not accurate.

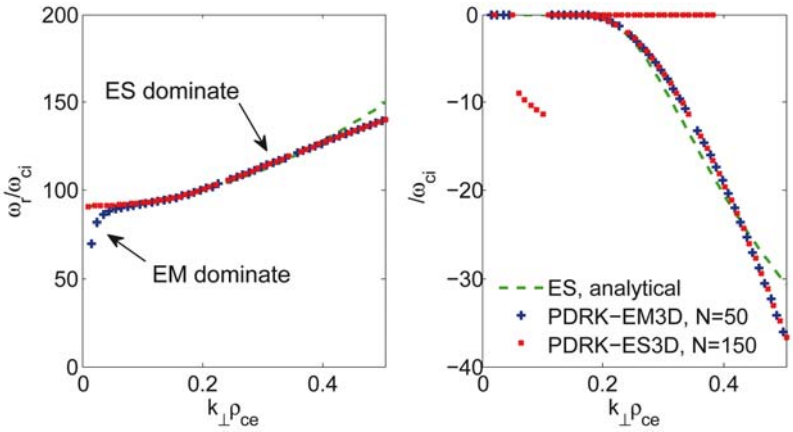

Fig.8 Landau damping of lower hybrid wave. Solutions from PDRK-ES3D (red, $N = 150$), PDRK-EM3D (blue, $N = 50$), and the analytical solution (dash green line) in Ref. [21]. It took about 1 CPU hour to compute the data in this figure

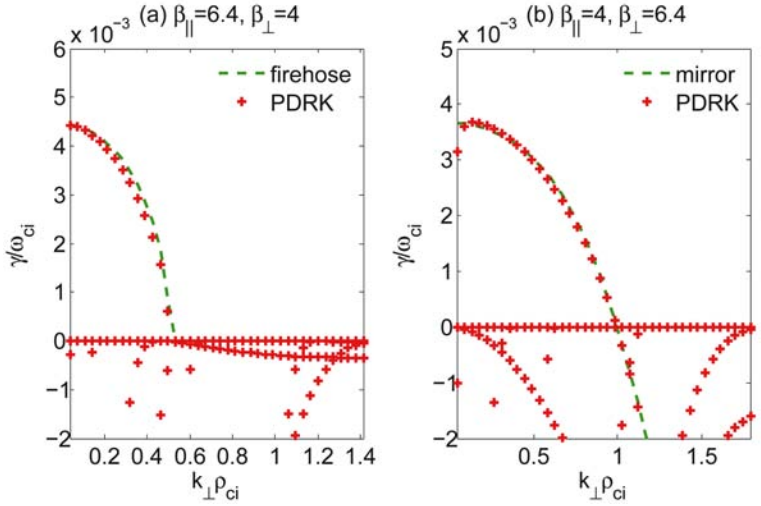

Fig.9 Growth rates for the firehose and mirror modes vs. $k_\perp\rho_\mathrm{ci}$. The dashed green lines in (a) an (b) are analytic solutions for firehose or mirror modes respectively

4.5 Whistler beam mode

The beam $v_{s0} \neq 0$ can also drive instabilities. We benchmark the whistler beam mode here. The parameters are similar to Fig. 8.8 of Ref. [5], with s=b,c,i, $m_\mathrm{i}/m_\mathrm{e} = 1836$, $n_\mathrm{i} = 1.0\mathrm{e}4$, $n_\mathrm{b} = 0.1n_\mathrm{i}$, $n_\mathrm{c} = 0.9n_\mathrm{i}$, $T_\mathrm{c} = T_\mathrm{i} = T_\mathrm{b}/10 = 0.5556$ and $v_{\mathrm{b}0} = -9v_{\mathrm{c}0} = 2.108$, which yield $\omega_\mathrm{pe} = 100\omega_\mathrm{ce}$, $\beta_\mathrm{c} = 1.0$ and $v_{\mathrm{b}0} = 2.0v_{tc}$, where β_c is the background plasma β. The ω and γ vs. (k_z, k_x) results are shown in Fig. 10. The most unstable mode is the parallel propagation mode ($k = k_\parallel$), which is consistent with Gary's conclusion [5].

4.6 Dispersion surface

The 2D structure of ω vs. (k_x, k_z) (dispersion surface [23]) is shown in Fig. 11 for electron Bernstein wave (EBW). This type of figure is helpful in displaying the fine structure of the dispersion relations in $(k_\perp, k_\parallel)$ space and in revealing the relations among different modes. It is clearly shown in Panel (b) that the solutions are separated by cyclotron frequencies, i.e., the solution $n\omega_\mathrm{c} < \omega < (n{+}1)\omega_\mathrm{c}$ ($n = 0, 1, 2, ...$) exists for any k. In Fig. 11, we only keep $N = 10$, and both real and artificial solutions are shown. To see the fine structure of the real solutions more clearly, further processing is required to remove the artificial solutions, which is the main disadvantage of the present version of PDRK.

4.7 Others

In the above benchmarks, no apparent numerical problems are found. However, this does not mean that we can apply PDRK for all cases because only approximations of Z function are used. In WHAMP [2], the Z function is also approximated by J-pole expansion. A further approximation is taken for the Bessel function summation. Thus, in principle, PDRK-EM3D will give more accurate results than WHAMP. Similar issues regarding the validity of Padé approximation for Z is discussed in detail in the WHAMP report [2]. Based on our results, the error for $J = 8$ is less than 10^{-4}, which may bring some artificial growing modes. If the same solution also exists for other J (e.g., $J = 4, 12$), it is more likely to be a real solution. Otherwise, care should be exercised in treating this solution. We can distinguish real and artificial solutions by using different J. The artificial solutions change when J changes. In contrast, the real solutions do not change that much.

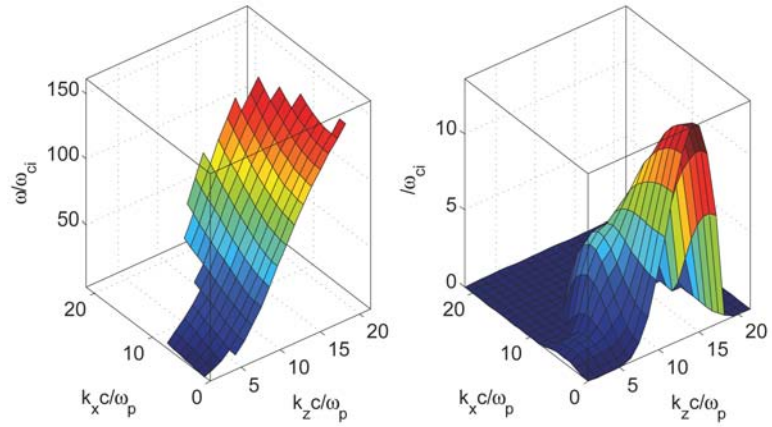

Fig.10 Electromagnetic whistler beam instability. The real frequency ω is only shown for unstable ($\gamma > 0$) solutions. The parallel propagation ($k = k_\parallel$) results are similar to Fig.8.8 of Ref. [5]. $N = 3$ is used for this calculation

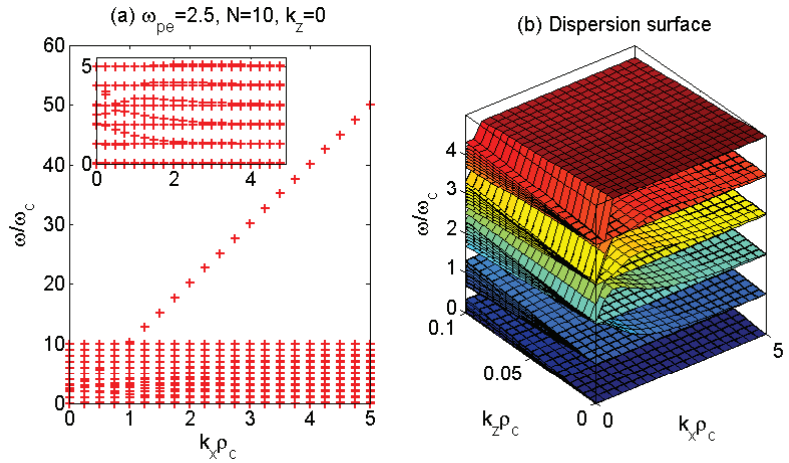

Fig.11 Dispersion surface (b) from PDRK-EM3D, using the EBW parameters in Fig. 3 and $c^2 = 10^2$. The ω vs. $k_\perp$ (a) result is close to the ES3D result in Fig. 3, which confirms that EBW is (quasi-) electrostatic

5 Summary and discussion

A general, fast, and effective approach is developed for numerical calculation of kinetic plasma dispersion relations based on Padé approximation and matrix transformation. And, this method is implemented in a general kinetic plasma dispersion relation solver, PDRK, where the equilibrium distribution function is assumed to be drift bi-Maxwellian. For other non-Maxwellian distribution functions, the J-pole expansion (Appendix A) of the corresponding new Z functions [14] should be obtained first. Note that the relativistic effect (e.g., Refs. [24-26]) is not included in the present study as this would make the solution more complicated. However, in principle, it can also be treated using Padé approximation [25]. Further improvements of the present method to treat the dispersion relations without infinite Bessel function summation (e.g., Ref. [27]) or with ring-beam velocity distributions (e.g., Ref. [28]) would also be interesting. Although PDRK is more accurate than PDRF, the latter is still advantageous in some cases because it can handle more configurations, such as relativistic systems, local non-uniform systems, and systems where collisions are considered. For practical applications, one can use PDRF to obtain rough solutions, and then use these to provide initial guesses for PDRK or use them for assistance in removing the artificial solutions in PDRK. Besides the multi-fluid model, PDRK also provides a tool to check the validity of other reduced models, such as Darwin [20] and gyro-kinetic [9,29] models.

For systems with small N (e.g., $N < 60$ for two species) or unstable modes, PDRK works excellently and is applicable to most cases used. For large N (e.g., $N > 60$), especially in studying the effect of $n\Omega_c$ the modes (e.g., LHW), the performance of PDRK is limited mainly by the computational time and memory. However, this concern may be remedied by using sparse matrices. Further optimization is possible. For example, we do not need to treat N equally for each species, e.g., for LHW, we can use large N_i but small N_e. The main disadvantage of PDRK is that artificial solutions originate from the poor approximation for strongly damped modes.

Compared with conventional solvers, the PDRK method/solver is fast and can give all solutions. Therefore, no important solutions are missed. It is also free from convergence problems. Hence, this method and solver can find wide applications in space, astrophysical, laser, and laboratory plasma studies.

Mathematically, after Padé approximation, this matrix transformation method is similar to find a companion matrix to a rational function. In linear algebra, there only exists standard form of the companion matrix for a polynomial function. Thus, the present work may also inspire some general theory for the companion matrix to rational functions.

Appendix A: Arbitrary J-pole expansion

The J-pole expansion coefficients b_j and c_j are provided only for small J in literature. Here, based on the study of Ronnmark [2], we develop a scheme to calculate numerical coefficients for any J. This is possible because we do not need analytical expressions. The J-pole expansion is

$$Z(\zeta) \simeq Z_{\rm A}^J(\zeta) = \frac{\sum_{k=0}^{J-1} p_k \zeta^k}{q_0 + \sum_{k=1}^{J} q_k \zeta^k}, \tag{14}$$

with $q_0 = 1$, it should be matched with the following two-side approximation

$$Z(\zeta) \simeq \begin{cases} \sum_{k=0}^{\infty} a_k \zeta^k & \simeq {\rm i}\sqrt{\pi}{\rm e}^{-\zeta^2} - \zeta \sum_{n=0}^{\infty} (-\zeta^2)^n \frac{\Gamma(1/2)}{\Gamma(n+3/2)}, \quad \zeta \to 0 \\ \sum_{k=0}^{\infty} a_{-k} \zeta^{-k} & \simeq {\rm i}\sigma\sqrt{\pi}{\rm e}^{-\zeta^2} - \sum_{n=0}^{\infty} \frac{\Gamma(n+1/2)}{\Gamma(1/2)\zeta^{2n+1}}, \quad \zeta \to \infty \end{cases} \tag{15}$$

where

$$\sigma = \begin{cases} 0, & {\rm IM}(\zeta) > 0, \\ 1, & {\rm IM}(\zeta) = 0, \\ 2, & {\rm IM}(\zeta) < 0, \end{cases} \tag{16}$$

and Γ is Euler's Gamma function. A further expansion is ${\rm e}^{-\zeta^2} = \sum_{n=0}^{\infty} \frac{\zeta^{2n}}{n!}$. However, ${\rm i}\sigma\sqrt{\pi}{\rm e}^{-\zeta^2}$ is omitted, which does not match well for the range $y < \sqrt{\pi}x^2{\rm e}^{-x^2}$ when $x \gg 1$. The system of equations to be solved are

$$p_j = \sum_{k=0}^{j} a_k q_{j-k}, 1 \le j \le I \tag{17a}$$

$$p_{L-j} = \sum_{k=0}^{j} a_{-k} q_{L+k-j}, 1 \le j \le K \tag{17b}$$

where $I + K = 2J$, and $p_j = 0$ for $j > J-1$ and $j < 0$, and $q_j = 0$ for $j > J$ and $j < 0$. Thus $2J$ equations determine $2J$ coefficients p_j and q_j in (14). The derivation of (17) is similar to that of Eqs. (III-5) and (III-7) in Ronnmark [2]. Eqs. (17) are solved using matrix inversion. The 'residue' function in MATLAB is used to calculate b_j and c_j in (2) from (14). The results for $J = 12$ using $I = 16$ equations of (17a) and $K = 8$ equations of (17b) are given in Table 1.

Usually, a large J gives better approximations. However, this is not always the case. Test should be made before using them. Moreover, the truncated error when using double precision data can accumulate to 10^{-11}.

Calculating the J-pole expansions for other equilibrium distribution functions [14] is also straightforward. We merely replace the coefficients a_k and a_{-k} in (15).

Appendix B: Equivalent sparse matrix for ES1D system

As mentioned, the equivalent matrix from Eq. (4) for ES1D system is not sparse. An equivalent sparse matrix for ES1D system can be constructed as following:

$$\omega n_{sj} = c_{sj} n_{sj} + b_{sj} E, \tag{18a}$$

$$\omega E = -\sum_{sj} c_{sj} n_{sj} - \sum_{sj} b_{sj} E. \tag{18b}$$

This is similar by changing the ES1D Vlasov-Poisson system to the ES1D Vlasov-Ampere system [15]. Eq. (18b) can be further simplified to be $\omega E = -\sum_{sj} c_{sj} n_{sj}$, because $\sum_{sj} b_{sj} = 0$. The ES3D matrix in Sec. 2.2 can be changed to sparse matrix in a similar manner.

References

1 Xie H S. 2014, Computer Physics Communications, 185: 670
2 Ronnmark K. 1982, KGI Report, No. 179, Sweden
3 Ronnmark K. 1983, Plasma Physics, 25: 699
4 Verscharen D, Bourouaine S, Chandran B D G, et al. 2013, The Astrophysical Journal, 773: 8
5 Gary S P. 1993, Theory of Space Plasma Microinstabilities. Cambridge University Press, New York
6 Gary S P, Liu K, Winske D. 2011, Phys. Plasmas, 18: 082902
7 Willes A J, Cairns I H. 2000, Phys. Plasmas, 7: 3167
8 Verdon A L, Cairns I H, Melrose D B, et al. 2009, Phys. Plasmas, 16: 052105
9 Lin Y, Wang X Y, Lin Z, et al. 2005, Plasma Phys. Control. Fusion, 47: 657
10 Martin P, Donoso G, Zamudio-Cristi J. 1980, J. Math. Phys., 21: 280
11 Cereceda C, Puerta J. 2000, Phys. Scr., 2000: 206
12 Tjulin A, Eriksson A I, Andre M. J. 2000, Plasma Physics, 64: 287
13 Robinson P A, Newman D L. 1988, J. Plasma Phys., 40: 553
14 Xie H S. 2013, Phys. Plasmas, 20: 092125
15 Xie H S. 2013, Phys. Plasmas, 20: 112108
16 Gurnett D A, Bhattacharjee A. 2005, Introduction to Plasma Physics: with Space and Laboratory Applications. Cambridge University Press, Cambridge
17 Birdsall C, Langdon A. 1991, Plasma Physcis via Computer Simulation. IOP, New York
18 Gitomer S J, Forslund D W, Rudsinski L. 1972, Physics of Fluids, 15: 1570
19 Stix T. 1992, Waves in Plasmas. AIP Press, New York
20 Xie H S, Zhu J, Ma Z W. 2014, Phys. Scr., 89: 105602
21 Qi L, Wang X Y, Lin Y. 2013, Phys. Plasmas, 20: 062107
22 Bao J, Lin Z, Kuley A, et al. 2014, Plasma Phys. Control. Fusion, 56: 095020
23 André M. 1985, J. Plasma Phys., 33: 1
24 Bret A, Gremillet L, Bénisti D. 2010, Phys. Rev. E, 81: 036402
25 Hao B, Ding W J, Sheng Z M, et al. 2012, Phys. Plasmas, 19: 072709
26 Timofeev I V, Annenkov V V. 2013, Phys. Plasmas, 20: 092123
27 Qin H, Phillips C, Davidson R C. 2007, Phys. Plasmas, 14: 092103
28 Umeda T, Matsukiyo S, Amano T, et al. 2012, Phys. Plasmas, 19: 072107
29 Howes G G, Cowley S C, Dorland W, et al. 2006, The Astrophysical Journal, 651: 590

(Manuscript received 22 April 2015)
(Manuscript accepted 12 June 2015)
E-mail address of XIE Huasheng:
huashengxie@gmail.com